The Impact of Finite-Amplitude Bottom Topography on Internal Wave Generation in the Southern Ocean

MAXIM NIKURASHIN

Institute for Marine and Antarctic Studies, University of Tasmania, Hobart, and ARC Centre of Excellence for Climate System Science, Sydney, New South Wales, Australia

RAFFAELE FERRARI

Department of Earth, Atmospheric and Planetary Sciences, Massachusetts Institute of Technology, Cambridge, Massachusetts

NICOLAS GRISOUARD

Department of Environmental Earth System Science, Stanford University, Stanford, California

KURT POLZIN

Woods Hole Oceanographic Institution, Woods Hole, Massachusetts

ABSTRACT

Direct observations in the Southern Ocean report enhanced internal wave activity and turbulence in a kilometer-thick layer above rough bottom topography collocated with the deep-reaching fronts of the Antarctic Circumpolar Current. Linear theory, corrected for finite-amplitude topography based on idealized, two-dimensional numerical simulations, has been recently used to estimate the global distribution of internal wave generation by oceanic currents and eddies. The global estimate shows that the topographic wave generation is a significant sink of energy for geostrophic flows and a source of energy for turbulent mixing in the deep ocean. However, comparison with recent observations from the Diapycnal and Isopycnal Mixing Experiment in the Southern Ocean shows that the linear theory predictions and idealized two-dimensional simulations grossly overestimate the observed levels of turbulent energy dissipation. This study presents two- and three-dimensional, realistic topography simulations of internal lee-wave generation from a steady flow interacting with topography with parameters typical of Drake Passage. The results demonstrate that internal wave generation at three-dimensional, finite bottom topography is reduced compared to the two-dimensional case. The reduction is primarily associated with finite-amplitude bottom topography effects that suppress vertical motions and thus reduce the amplitude of the internal waves radiated from topography. The implication of these results for the global lee-wave generation is discussed.

1. Introduction

Recent observations show that internal wave kinetic energy and turbulent energy dissipation are enhanced up to a kilometer above rough bottom topography in the Southern Ocean (Polzin and Firing 1997; Naveira Garabato et al. 2004; Sloyan 2005; St. Laurent et al. 2012; Waterman et al.

2012). These observations suggest that enhanced turbulence is sustained by breaking internal waves generated when the strong bottom flows of the Antarctic Circumpolar Current (ACC) impinge on the rough bottom topography. The internal wave–driven turbulence greatly enhances the mixing of water masses in the ocean interior (e.g., Garrett and St. Laurent 2002) and hence contributes to the maintenance of stratification and associated meridional overturning circulation of the ocean (e.g., Munk and Wunsch 1998; Nikurashin and Vallis 2011).

Using linear lee-wave theory, Nikurashin and Ferrari (2011) produced an estimate of the global distribution of

Corresponding author address: Maxim Nikurashin, Institute for Marine and Antarctic Studies, University of Tasmania, Private Bag 129, Hobart, TAS 7001, Australia.
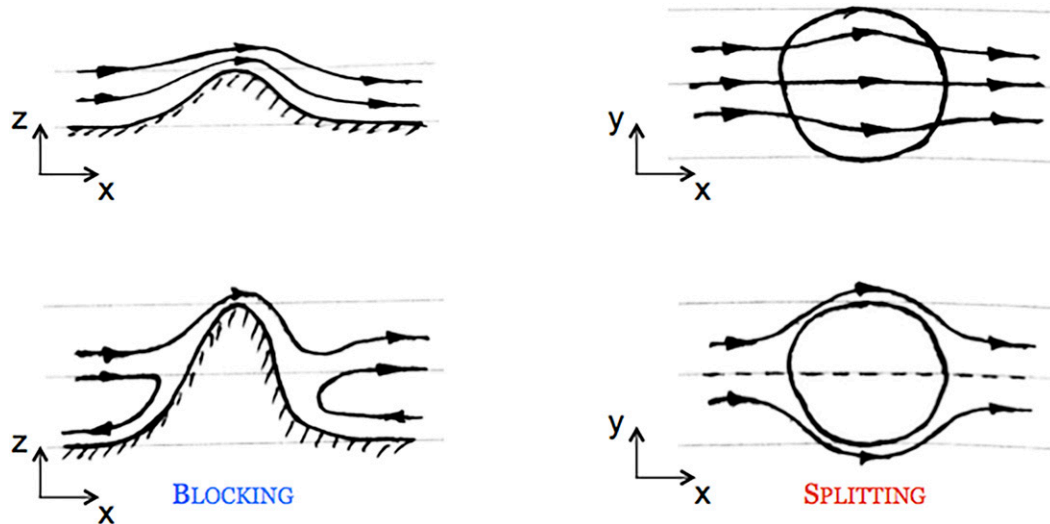E-mail: man@alum.mit.edu

FIG. 1. A sketch of the mean flow–topography interaction: (top) subcritical topography limit and (bottom) critical topography limit; (left) vertical plane view and (right) horizontal plane view. The bottom two panels illustrate the blocking and splitting effects arising in the critical topography limit.

internal wave generation by oceanic currents and eddies. The total energy conversion into lee waves was estimated to be 0.2 TW (1 TW = 10^{12} W) or about 20% of the total wind power input into the large-scale circulation of the ocean (e.g., Wunsch 1998). Roughly half of the total energy conversion takes place in the Southern Ocean, south of 40°S. Using the same theory but different estimates of the bottom flow and topography, Scott et al. (2011) found a higher global energy conversion into lee waves of 0.4 TW, also concentrated in the Southern Ocean. Nikurashin and Ferrari (2013) have recently combined the global energy conversion into lee waves with a mixing parameterization (St. Laurent et al. 2002) to produce a three-dimensional distribution of internal wave–driven diapycnal mixing. Applying this mixing to the observed density distribution in the ocean, Nikurashin and Ferrari estimate that the lee wave–driven mixing can accomplish a few Sverdrups (Sv; 1 Sv ≡ 10^6 m³ s⁻¹) of water mass transformation in the deep ocean.

The linear theory used to make these global estimates is formally valid in a limit of subcritical topography, that is, when the topographic height is smaller than the vertical internal wave scale (e.g., Bell 1975a,b). The criticality of topography is characterized by the steepness parameter:

$$s = \frac{hN}{U}, \qquad (1)$$

where h is the characteristic topographic height, and U/N is the characteristic vertical scale of lee waves given by the ratio of the mean velocity and the buoyancy frequency at

the ocean bottom. In the case of lee waves, where the wave horizontal scale is set by the horizontal scale of topography, this definition is equivalent to the one used for oscillating flows (e.g., Bell 1975a,b). Most of the topography in the Southern Ocean varies from subcritical to critical (Nikurashin and Ferrari 2011), with topographic steepness parameters of $O(1)$. In the critical topography limit, when the linear theory is not formally valid, the global predictions for the energy conversion are corrected empirically based on idealized two-dimensional (2D) numerical simulations (e.g., Nikurashin and Ferrari 2010a) and laboratory experiments (e.g., Aguilar and Sutherland 2006). The idealized 2D simulations and idealized 2D laboratory experiments show that when the steepness parameter exceeds a critical value of 0.7–0.8, the energy conversion saturates, that is, it ceases to increase for increasing topographic steepness. The saturation occurs because a certain fraction of the mean flow does not have enough kinetic energy to overcome an obstacle, becomes blocked by topography, and does not lift isopycnals to generate internal waves (Fig. 1). Scott et al. (2011) discussed various empirical corrections to taper the linear energy conversion at supercritical topography and found that results are insensitive to the form of the tapering function, but are sensitive to the critical steepness parameter. In this study, we will show that the critical steepness parameter of 0.7–0.8 used in published lee-wave generation estimates is not appropriate when one considers three-dimensional (3D) topographic effects.

Recent direct turbulence measurements from the Diapycnal and Isopycnal Mixing Experiment (DIMES) in the Drake Passage region (St. Laurent et al. 2012)

report a vertically integrated energy dissipation of up to $5\,\text{mW}\,\text{m}^{-2}$ from microstructure profiles collected in the Polar Front of the ACC. Profiles collected outside the ACC fronts show energy dissipation rates two orders of magnitude smaller with no enhancement near topography. In contrast, the idealized 2D simulations designed with parameters typical of the Polar Front region of Drake Passage (Nikurashin and Ferrari 2010a,b) radiated $80\,\text{mW}\,\text{m}^{-2}$ of internal waves from the bottom topography (consistent with linear theory predictions), resulting in a vertically integrated dissipation of $25\,\text{mW}\,\text{m}^{-2}$. These numerical simulations do not fully resolve internal wave breaking and the resulting turbulence down to the viscous dissipation scale. However, they simulate the flux of internal wave energy toward smaller scales, where it is removed by the numerical dissipation scheme. To the extent that in nature the energy flux progresses all the way down to the molecular dissipation scale, the flux can be used as a proxy for dissipation, which is the same assumption made in dissipation estimates based on finescale estimates of shear and stratification on vertical scales of 10–100 m (e.g., Waterman et al. 2012). The 2D simulations overestimate dissipation also outside the fronts, but disagreement is less of a concern because the values are very small in both observations and simulations. A similar disagreement between linear theory estimates and direct energy dissipation measurements has also been reported in the region of the Southern Ocean Finestructure (SOFine) experiment north of Kerguelen Plateau (Waterman et al. 2012).

There are a number of mechanisms that could explain the disagreement between linear theory, 2D simulations, and observations: there are large uncertainties in the local topography spectrum needed to estimate the wave generation and dissipation; finite topography effects, such as flow blocking and splitting, are neglected in the linear theory and possibly misrepresented in 2D simulations; modulation of the wavefield by and energy exchanges associated with shears and strains of the mean flow are ignored; the energy balance may be nonlocal because of the remote breaking of lee waves; and the turbulence may be undersampled in observations because of the highly intermittent character of turbulent energy dissipation. New observations will be needed to address the impact of uncertainties in the topographic spectrum and the sampling of turbulent energy dissipation. Numerical simulations can be used to test whether the assumption built in the theory properly describes the full 3D radiation problem. We initiate this effort here.

There is a rich atmospheric literature suggesting that wave radiation by finite-amplitude 3D topography is strongly suppressed compared to the 2D limit (e.g., Miranda and James 1992; Baines and Smith 1993; Welch et al. 2001; Epifanio and Durran 2001; Eckermann et al. 2010). While the flow can become blocked by topography both in 2D and 3D, in 3D the flow can also split and go around topographic obstacles rather than over them (Fig. 1). The flow component going around the obstacles does not lift isopycnals and hence does not generate internal waves. Based on these results, it seems worthwhile to assess the impact of finite topography effects, such as blocking and splitting, on the radiation of internal waves in the Southern Ocean. While 3D effects may not be the only reason for the discrepancy between observations and 2D simulations, they potentially contribute to the overestimation of turbulent dissipation rates.

In the rest of the paper we use a suite of 2D and 3D simulations to explore the finite-amplitude effects on internal wave generation for realistic, multiscale abyssal hill topography and flow characteristics observed in the Drake Passage region of the Southern Ocean. We also use the results of the 3D simulations to update the global estimate of the energy conversion into lee waves for finite-amplitude topography effects.

2. Methods

The interaction of a mean flow with topography and the generation of lee waves are explored here using 2D and 3D simulations. We design the reference simulations with parameters typical of the Polar Front of the ACC in Drake Passage. To study the effects of finite-amplitude topography, we explore a wide range of topographic steepness parameter from subcritical to critical limits by varying the amplitude of the bottom topography.

a. Characteristics of the Polar Front of the ACC in Drake Passage

This study focuses on the Polar Front of the ACC in Drake Passage because it is characterized by the strongest bottom velocities in the region and hence dominates the regional wave generation and energy dissipation by a few orders of magnitude (Nikurashin and Ferrari 2010b; St. Laurent et al. 2012). Compared to other sectors of the Southern Ocean, Drake Passage is well sampled by observations: measurements are available for high-resolution, two-dimensional topography, geostrophic flow and stratification, internal waves, and turbulence (Naveira Garabato et al. 2003, 2004; Nikurashin and Ferrari 2010b; St. Laurent et al. 2012). To choose characteristic mean flow and stratification for the simulations and to compare the simulation results against the observed, vertically integrated dissipation rates, we used recent observations in Drake Passage from DIMES (St. Laurent et al. 2012). The location of microstructure,

velocity, and stratifications measurements are shown in Fig. 2 and the mean flow and stratification profiles are shown in Fig. 3. The profiles are averaged in a height-above-bottom vertical coordinate over a few stations in the vicinity of the Polar Front, as indicated in Fig. 2.

The mean flow stratification frequency in this region is roughly $10^{-3}\,\mathrm{s}^{-1}$ in the bottom kilometer and increases by about a factor of 2 between 1 and 2 km above the bottom. The mean speed near the bottom is $10\,\mathrm{cm\,s}^{-1}$ and increases to $20\text{–}30\,\mathrm{cm\,s}^{-1}$ between 1 and 2 km above the bottom. For these values of bottom stratification and flow speed, a hydrostatic, nonrotating linear theory predicts the vertical wavelength of lee waves of $2\pi U/N \approx 600\,\mathrm{m}$. Hence, the mean stratification and flow speed are effectively constant over the characteristic vertical wavelength of lee waves. Consistently, in the simulations, we impose uniform mean flow and stratification with values of $10\,\mathrm{cm\,s}^{-1}$ and $10^{-3}\,\mathrm{s}^{-1}$, respectively. The variations of the mean flow with height will impact the evolution of lee waves and the resulting turbulent energy dissipation (e.g., Waterman et al. 2012). However, the processes governing internal wave evolution, including wave–wave and wave–mean flow interactions, are outside the scope of this study and will be addressed in future work. Here, the focus is on wave generation.

The observed enhanced turbulence and mixing have been suggested to be associated with breaking internal waves (e.g., St. Laurent et al. 2012; Waterman et al. 2012). Therefore, the large dissipation rates in the bottom kilometer are likely associated with waves that break close to the region where they are radiated away from topography. Thus an accurate estimation of lee-wave generation in 3D is an essential step in understanding the relation between the energy flux associated with lee-wave generation and the near-bottom dissipation rates associated with lee-wave breaking.

b. The effective one-dimensional spectrum of topography

Twin simulations in 2D and 3D are configured with topographies that would lead to identical energy conversion into lee waves according to linear theory, as
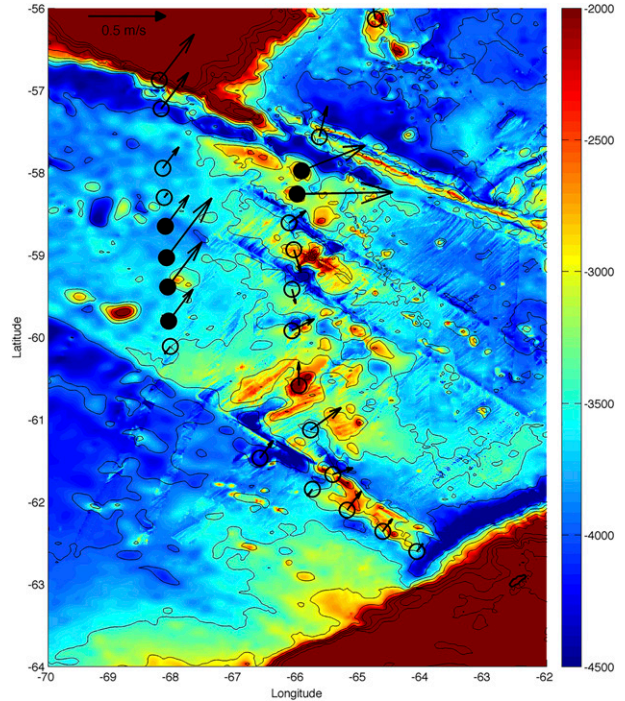

FIG. 2. Bathymetry of the Drake Passage region in meters showing the location of the DIMES stations from the Antarctic Large-Scale Box Analysis and the Role of the Scotia Sea (ALBATROSS) and Phoenix Ridge sections. Vectors show the observed flow averaged in the top 500 m as measured by lowered acoustic Doppler current profiler (LADCP). The solid dots indicate the stations with LADCP, CTD, and microstructure measurements (St. Laurent et al. 2012) chosen for the model setup and validation, characterized by strong surface flows corresponding to the Polar Front of the ACC.

explained in detail below. Hence, any differences in wave generation between the 2D and 3D twin experiments are expected to arise because of finite-amplitude topography effects.

Lee waves are generated by a steady current flowing over rough bottom topography in a stratified fluid. In the limit of subcritical topography, linear theory (Bell 1975a,b) shows that the energy conversion E from the mean flow into lee waves is given by

$$E = \frac{\rho_0}{4\pi^2} \int_{-\infty}^{+\infty} \int_{-\infty}^{+\infty} P_{2\mathrm{D}}(k,l)\frac{(\mathbf{U} \cdot \mathbf{k})}{|\mathbf{k}|} \sqrt{N^2 - (\mathbf{U} \cdot \mathbf{k})^2}\sqrt{(\mathbf{U} \cdot \mathbf{k})^2 - f^2}\,dk\,dl, \tag{2}$$

where $\mathbf{k} = (k,l)$ is the wavenumber vector, $P_{2\mathrm{D}}(k,l)$ is the 2D topographic spectrum, $\mathbf{U}$ is the bottom velocity vector, f is the Coriolis frequency, N is the bottom stratification, and ρ_0 is a reference density. Hence, the energy conversion at each topographic wavenumber depends on the

magnitude of the topographic spectrum and the relative orientation of the velocity and wavenumber vectors, given by $(\mathbf{U} \cdot \mathbf{k})$. Without a change in the energy radiation, the reference frame can be rotated to have the k axis along the velocity vector $\mathbf{U}$ and the expression for E reduces to
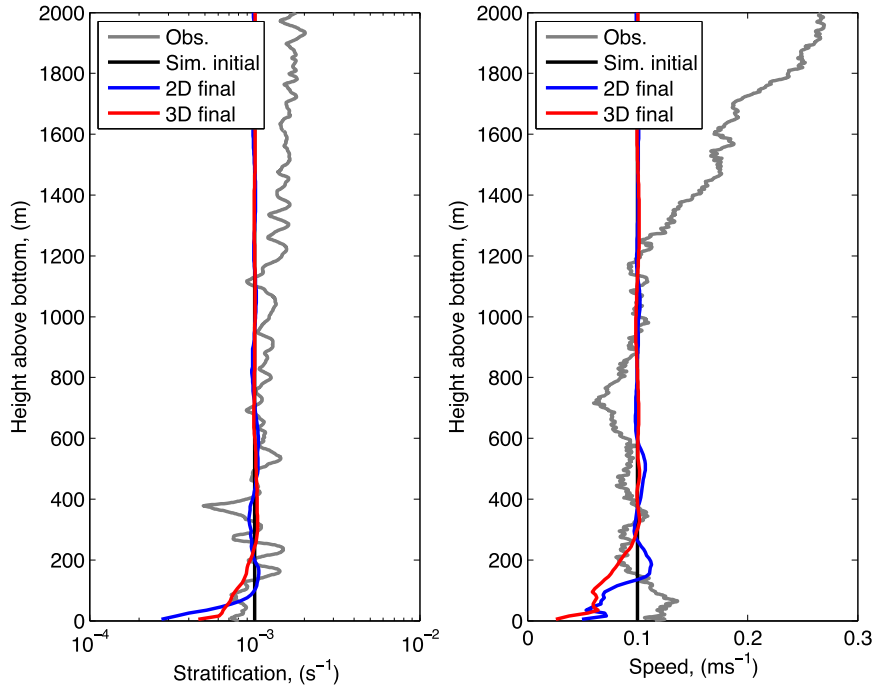
FIG. 3. Averaged profiles of (left) stratification (s^{-1}) and (right) flow speed ($m\,s^{-1}$) in the bottom 2 km from observations (gray), initial condition in the simulations (black), and final state in 2D (blue) and 3D (red) simulations.

$$E = \frac{\rho_0 |\mathbf{U}|}{\pi} \int_{|f|/|\mathbf{U}|}^{N/|\mathbf{U}|} P_{1D}(k) \sqrt{N^2 - |\mathbf{U}|^2 k^2} \sqrt{|\mathbf{U}|^2 k^2 - f^2}\, dk,$$

$$(3)$$

where $\mathbf{k} = (k, l)$ is now the wavenumber in the reference frame along and across the mean flow $\mathbf{U}$ and

$$P_{1D}(k) = \frac{1}{2\pi} \int_{-\infty}^{+\infty} \frac{|k|}{|\mathbf{k}|} P_{2D}(k, l)\, dl \qquad (4)$$

is the effective one-dimensional (1D) topographic spectrum. Hence, the wave radiation from 2D topography reduces to an equivalent problem of wave radiation from 1D topography with the effective spectrum given by $P_{1D}(k)$.

The effective 1D spectrum captures the effects of 2D topography on lee-wave radiation in the subcritical topography limit, that is, $P_{2D}(k, l)$ and $P_{1D}(k)$ result into identical radiation estimates for small steepness parameters. However, the suppression of wave radiation in the critical topography limit is different in 1D and 2D; 1D critical topography leads to blocking of the mean flow, while in 2D both blocking and splitting of the mean flow can occur. Hence, the radiation from $P_{2D}(k, l)$ and $P_{1D}(k)$ is expected to diverge as the topographic steepness is increased.

c. Bottom topography

Simulations are configured with multiscale topography characterized by small-scale abyssal hills a few kilometers wide based on multibeam observations from Drake Passage. The topographic spectrum associated with abyssal hills is well described by an anisotropic parametric representation proposed by Goff and Jordan (1988):

$$P_{2D}(k, l) = \frac{2\pi H^2 (\mu - 2)}{k_0 l_0} \left(1 + \frac{k^2}{k_0^2} + \frac{l^2}{l_0^2} \right)^{-\mu/2}, \qquad (5)$$

where k_0 and l_0 set the wavenumbers of the large hills, μ is the high-wavenumber spectral slope, related to the parameter ν used in Goff and Jordan (1988) as $\mu = 2(\nu + 1)$, and H is the root-mean-square (rms) topographic height. Nikurashin and Ferrari (2010b) estimated with a least squares fit to multibeam data that representative values in the Drake Passage region are $k_0 = 2.3 \times 10^{-4}\,m^{-1}$, $l_0 = 1.3 \times 10^{-4}\,m^{-1}$, $H = 305\,m$, and $\mu = 3.5$. Given that the abyssal hills are only slightly anisotropic with a horizontal aspect ratio of $k_0/l_0 \approx 1.8$, we hereinafter assume that the topography is isotropic and characterized by the averaged rolloff wavenumber $k_0 = l_0 = 1.8 \times 10^{-4}\,m^{-1}$. The

isotropic assumption was found to have little effect on the averaged wave energy conversion in Drake Passage as reported by Nikurashin and Ferrari (2010b). This assumption is made here essentially to estimate the time-mean lee-wave generation when fronts and eddies in the ocean change direction and strike topography at different angles—this is a valid estimate for eddies but likely less so for ACC fronts that tend to have a preferred direction. Exploring the role of anisotropy for the energy conversion in the finite energy limit in 3D is computationally expensive—so not considered here—but will be explored in the future.

Synthetic 2D and 1D topographies are computed as a sum of Fourier modes with random phases and spectral amplitudes given by (4) and (5), respectively. The 2D topography used in the simulation with parameters representative of Drake Passage is shown in Fig. 4. According to linear theory in (3), lee waves radiate from topographic wavelengths λ_T in the range

$$2\pi \frac{|\mathbf{U}|}{N} < \lambda_T < 2\pi \frac{|\mathbf{U}|}{|f|}. \tag{6}$$

For the Drake Passage parameters, this range includes horizontal wavelengths from roughly 600 m to 6 km. Scales shorter than 600 m and longer than 6 km generate evanescent waves. To focus on the radiating lee waves that can propagate energy away from topography and drive mixing in the ocean interior, we include topographic wavelengths from 300 m to 6 km in the simulations. Limited computational resources dictate this truncated topographic representation. Topographic variability at larger scales may preferentially orient the low-level flow and impact the net energy transfer.

The corresponding 1D topographic spectrum is normalized to return identical energy conversion rates in the subcritical limit. This normalization leads to different topographic rms heights: 50 m for 1D and 80 m for 2D topography. The rms heights differ by a factor of 1.6, which is roughly consistent with a factor of $\sqrt{2}$ difference from the definition of the effective topographic spectrum in (4). The ratio is not exact because each topography is a random realization of its spectrum. To explore subcritical and critical radiation regimes in the sensitivity study below, the amplitude of the topography is rescaled, while its shape is kept the same.

To characterize the criticality of topography for lee-wave generation in the simulations, we use the steepness parameter in (1) with the characteristic height h estimated as the rms topographic height corresponding to the 2D topographic spectrum in (5). This definition is consistent with the definitions used in the recent, global, lee-wave generation estimates (Nikurashin and
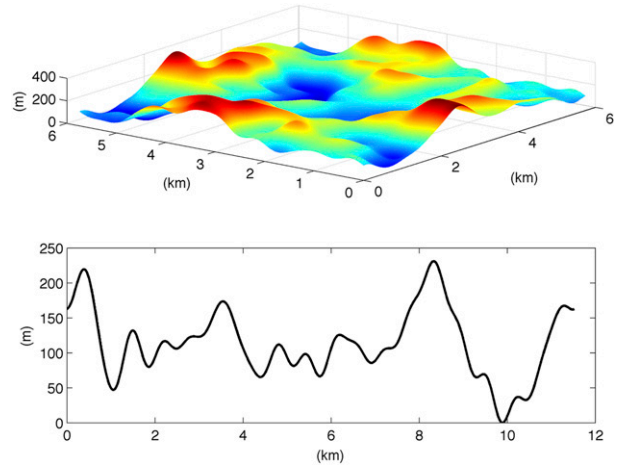

FIG. 4. Bottom topography (m) used in (top) 3D and (bottom) 2D simulations. There are no contributions from horizontal wavelengths larger than 6 km in 1D and 2D topographies.

Ferrari 2011; Scott et al. 2011). The reference simulation presented below has a steepness parameter of 0.8, consistent with previous Drake Passage steepness parameter estimates (Nikurashin and Ferrari 2010a,b).

d. Model configuration

We employ the Massachusetts Institute of Technology general circulation model (MITgcm) (Marshall et al. 1997). This model has been widely used for studies of topographic internal wave generation in the ocean (e.g., Khatiwala 2003; Legg and Klymak 2008; Nikurashin and Ferrari 2010a,b; Nikurashin et al. 2012). The design of the numerical experiments is similar to that in Nikurashin and Ferrari (2010a,b). This configuration of the model is also similar to those used in studies of wind–topography interaction in the atmospheric literature with idealized and isolated shapes of topographic obstacles (e.g., Welch et al. 2001; Epifanio and Durran 2001; Eckermann et al. 2010).

We use a resolution of $\Delta x = 40$ m in the horizontal and $\Delta z = 10$ m in the vertical in all simulations. This resolution is fine enough to resolve the smallest scale in topography and the characteristic lee-wave vertical scale. A no-slip boundary condition at the bottom is used in both 2D and 3D simulations. To test the sensitivity of the energy conversion to the choice of the bottom boundary condition, we also carry out 2D simulations with free-slip and free-slip with a quadratic bottom drag boundary conditions using a drag coefficient $C_D = 2 \times 10^{-3}$. A constant mean flow of $U = 0.1$ m s^{-1} is forced by adding a body force to the meridional momentum equation, representing a barotropic pressure gradient geostrophically balanced by the mean flow U at all depths. A uniform stratification of $N = 10^{-3}$ s^{-1} and a Coriolis frequency of

$f = -1.2 \times 10^{-4}\,\mathrm{s}^{-1}$ are used. The magnitude of the mean flow and stratification are chosen based on observations in Drake Passage (Naveira Garabato et al. 2002, 2003; St. Laurent et al. 2012). We use sponge layers 1.2 km wide on the upstream and downstream sides of the domain to absorb radiating waves and maintain the prescribed mean flow and stratification near topography. In the sponge layers, buoyancy and momentum are restored to the mean flow conditions at the rate that gradually increases from $(4\,\mathrm{h})^{-1}$ to $(10\,\mathrm{min})^{-1}$. A rigid-lid top boundary condition, allowing for the reflection of internal waves at the upper boundary, is used. The horizontal and vertical viscosities are set to $\nu_h = 5 \times 10^{-2}\,\mathrm{m}^2\,\mathrm{s}^{-1}$ and $\nu_v = 2 \times 10^{-2}\,\mathrm{m}^2\,\mathrm{s}^{-1}$ respectively. An isotropic diffusivity of $\kappa_h = \kappa_v = 10^{-5}\,\mathrm{m}^2\,\mathrm{s}^{-1}$ is used. These values are chosen to ensure numerical stability of the model. While they are higher than molecular and typical oceanic background values,[1] they are sufficiently small that the Reynolds and Peclet numbers estimated at the characteristic lee-wave scale are of $O(10^3)$ and $O(10^6)$, respectively, and hence the lee-wave generation can be regarded as inviscid and adiabatic. All experiments are initiated from a state of rest and run for 10 days to a statistically steady state.

3. Results

In this section, we describe the reference simulations and compare them to recent observations in Drake Passage. We also describe the results from a series of 2D and 3D simulations for increasing steepness parameter to study how finite-amplitude topography affects wave radiation in Drake Passage. Based on these simulations, we update our estimate of the internal lee-wave generation throughout the global oceans to account for 3D effects previously ignored.

a. The reference Drake Passage simulations

Snapshots of the wave zonal velocity, defined here as a deviation from the prescribed zonal mean flow, are shown in Fig. 5 for the reference 2D and 3D simulations. Both in 2D and 3D the wave zonal velocity is characterized by a well-established lee-wave field with phase lines tilting against the mean flow. While the bottom topography is multiscale, the radiated waves are dominated by

3–4-km horizontal scales consistent with the linear theory prediction of Nikurashin and Ferrari (2011) and Scott et al. (2011). The vertical scale of lee waves is 400–500 m, consistent with rotating linear theory, but a bit shorter than a characteristic nonrotating lee-wave vertical scale of $2\pi U/N \approx 600\,\mathrm{m}$.

A remarkable difference between the 2D and 3D simulations is that the waves above topography are weaker in 3D. While in 2D the lee-wave velocities reach $0.1\,\mathrm{m\,s}^{-1}$, in 3D the velocities reach only about half that value. To illustrate this more quantitatively, we show domain averaged rms velocities in Fig. 6. The plot shows that horizontal velocities at all levels above topography are about a factor of 2 weaker in the 3D simulation than in the 2D one, while they are comparable in the bottom 200–400 m, levels below the peaks of the topography. This is also consistent with the horizontal wavenumber spectra estimated above topography in the direction along the mean flow (not shown) that suggest that the 3D simulation energy levels are lower than those in 2D simulations across the whole range of horizontal scales.

To demonstrate that the difference in wave amplitudes results from the difference in topography, we run an additional 3D simulation that uses the same topography as the 2D simulation, that is, a topography that varies only in one direction (Fig. 5). The simulation shows that while the waves in the 3D simulation with 1D topography are weakly 3D, because of small 3D buoyancy perturbations in the initial conditions, their amplitude is similar to that in the 2D simulation. This further confirms that the 2D simulation captures well the 3D dynamics, if the same topography is used in both.

The difference between 2D and 3D lee waves does not seem to be related to changes in mean flow and stratification over the period of the simulation. In Fig. 3, we show vertical profiles of the mean flow speed and stratification from the 2D and 3D simulations. While both mean speed and stratification are slightly reduced in the bottom 100–200 m in 2D and 3D, because of the impact of the low-level waves and turbulence, the difference in the mean flow speed and stratification between 2D and 3D simulations is minor, only 20%–30%, and thus cannot explain the factor of 2 suppression of wave amplitudes in the 3D simulation.

Following the analysis presented in previous studies (e.g., Nikurashin and Ferrari 2010b; Waterman et al. 2012; Sheen et al. 2013), we now compare the modeled energy conversion rates to the observed, vertically integrated energy dissipation estimates. The modeled energy conversion rates are defined as the vertical energy flux $\overline{p'w'}$, where the overbar is the zonal and time mean and p' and w' are deviations from the zonal mean, estimated at the first level

---

[1] The enhanced background value of viscosity that we use in our study can be regarded as the simplest parameterization of subgrid-scale turbulent energy dissipation. We ensure that the grid-scale energy is removed by this explicit friction rather than spurious numerical viscosity by ensuring that the grid Reynolds number, the ratio of momentum advection to friction at the grid scale is of $O(1\text{–}10)$.
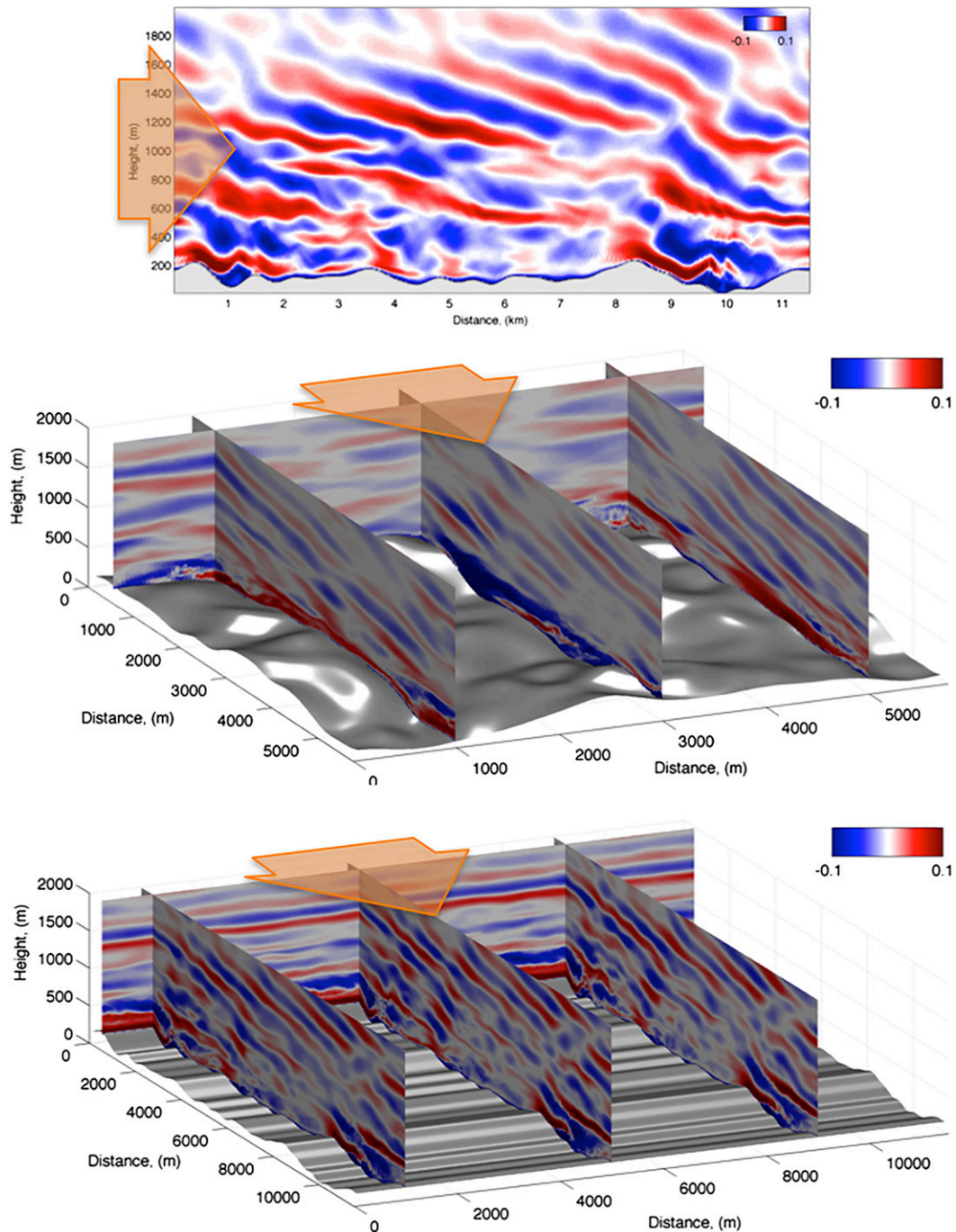
FIG. 5. Snapshots of the wave zonal velocity ($m\,s^{-1}$) from (top) 2D simulation, (middle) 3D simulation with 2D topography, and (bottom) 3D simulation with 1D topography. The direction of the mean flow is indicated with an arrow.

above the highest topographic bump. We focus here on the radiating part of the model solution and thus estimate the energy flux above the level of topography. Regions below the level of topography, that is, topographic valleys, are dominated by highly nonlinear processes in critical and supercritical simulations. The values of bottom energy conversion in the 2D and 3D simulations are about 10 and $50\,mW\,m^{-2}$. The observed, vertically integrated energy dissipation rates (St. Laurent et al. 2012) averaged over a few stations in the Polar Front of the ACC (Fig. 2) is about $3\,mW\,m^{-2}$. The comparison shows that the 2D model energy conversion
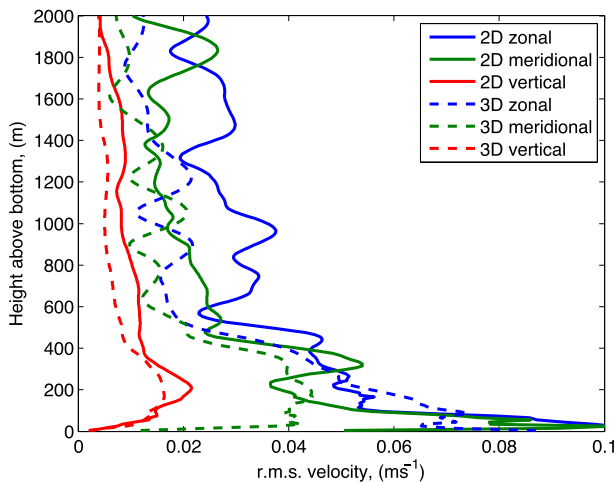
FIG. 6. Root-mean-square of the zonal (blue), meridional (green), and vertical (red) velocities (m s^{-1}) from 2D (solid) and 3D (dashed) simulations.

FIG. 7. Energy conversion into internal waves (mW m^{-2}) as a function of the topographic steepness parameter in (1) from 3D simulations with no-slip bottom boundary condition (asterisk) and 2D simulations with no-slip (square), free-slip (diamond), and drag (circle) bottom boundary conditions. Linear lee-wave theory scaling is shown with dashed black line.

rates are about an order of magnitude larger than the observed dissipation rates. In contrast, the 3D model energy conversion is a factor of 5 smaller than the 2D one and hence is more consistent with observations. It still overestimates the observed dissipation by about a factor of 3. This suggests that 3D finite topography effects significantly suppress the wave generation at the bottom and explain most of the discrepancy between observational and theoretical estimates. Other mechanisms must be less important.

b. Sensitivity to topographic steepness

A series of simulations with a steepness parameter spanning the transition from subcritical to critical topography regimes are now examined to study the differences between the wave radiation in 2D and 3D. In practice, we vary the rms height of the topography, while keeping its shape and examine the relative importance of 2D and 3D finite-amplitude topography effects as the rms height is increased. The energy conversion into lee waves diagnosed from 2D and 3D simulations is shown in Fig. 7 as a function of the steepness parameter defined in (1).

In the subcritical topography limit, the energy conversion estimates from the 2D and 3D simulations are similar. This is expected because the effective 1D topography was generated from the 2D topography to produce equivalent rates of the energy conversion in this limit. Consistent with the linear theory, the energy conversion in both 2D and 3D simulations scales quadratically with the topographic steepness parameter in the subcritical limit. In the critical topography limit, on the other hand, the energy conversion estimates from 2D and 3D simulations saturate, that is, cease to increase with topographic
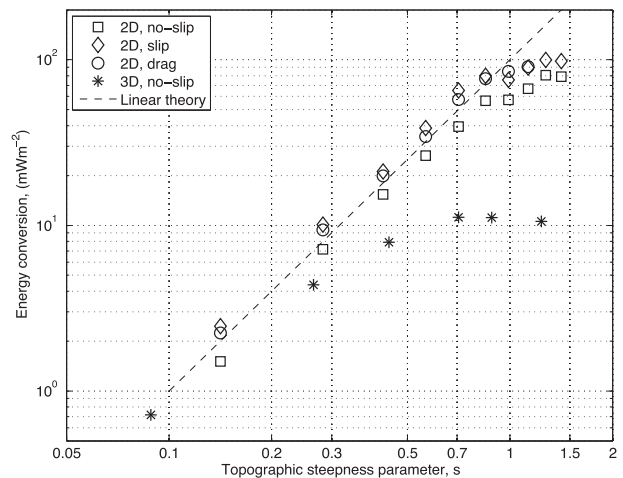
steepness. The simulation results strongly suggest that the saturation is due to nonlinear finite-amplitude topography effects. In the 2D simulations at a certain value of the steepness parameter, the 1D topography becomes steep enough to block the flow and prevent it from generating internal waves. In the 3D simulations, the 2D topography in addition splits the upstream flow and forces it to go around topographic obstacles rather than over them, also suppressing the generation of internal waves.

Figure 7 shows that the transition from subcritical to critical topography occurs at different values of the steepness parameter in 2D and 3D simulations. While the energy conversion in the 2D simulations saturates at a critical steepness parameter of about 0.7, in the 3D simulations it saturates at a smaller value of 0.4. We hypothesize that the difference between 2D and 3D simulations is primarily due to the nonlinear splitting effects that are present in the 3D simulations but completely absent from the 2D simulations. This results in a drop of a factor of 5 in the energy conversion from 2D to 3D for the Drake Passage steepness parameter. In other words, in the critical topography limit of Drake Passage, the 2D simulations radiate up to 5 times more energy into lee waves compared to the 3D simulations.

The bottom boundary condition also affects the lee-wave generation in the simulations. The no-slip bottom boundary condition causes flow separation on the lee side of topographic obstacles and has been shown to reduce the amplitude of radiated lee waves and therefore the
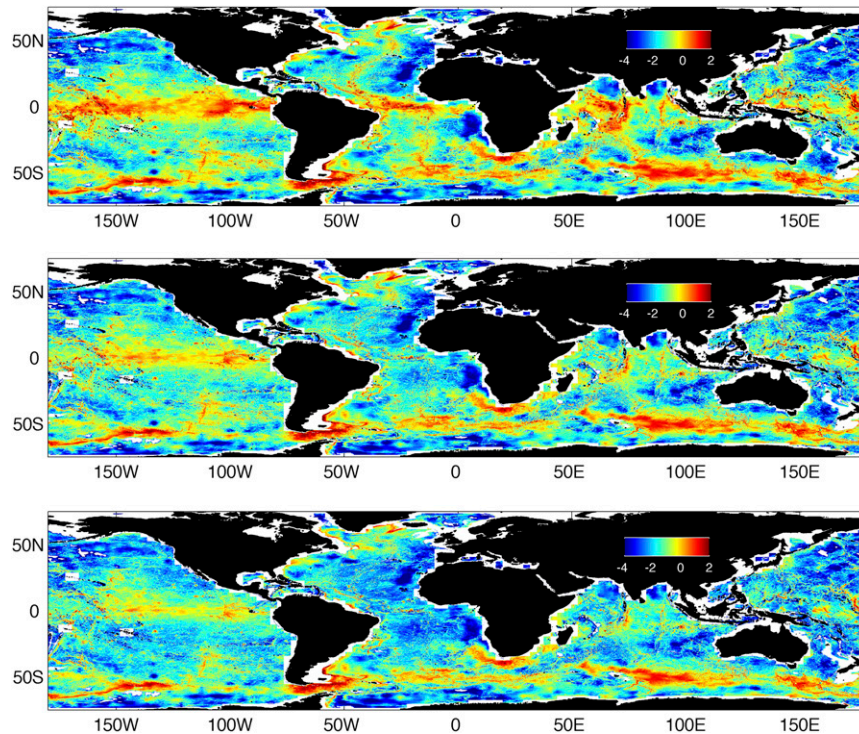
FIG. 8. Global time-averaged energy conversion into internal lee waves $[\log_{10}(\mathrm{mW\,m^{-2}})]$ (top) unadjusted to finite-amplitude topography, (middle) adjusted with the critical value of 0.7 based on 2D simulations, and (bottom) adjusted with the critical value of 0.4 based on 3D simulations.

magnitude of the bottom energy conversion by 20%–30% (Nikurashin and Ferrari 2010a). To test whether it affects our results on the saturation in the simulations here, we run 2D simulations with no-slip, free-slip, and free-slip with quadratic bottom drag boundary conditions (Fig. 7). The results show that while the bottom boundary condition makes an impact on the wave radiation with larger energy conversion in the simulations with a free-slip boundary condition, the impact is only on the order of 30% and does not affect the results of the finite-amplitude topography effects presented in this study.

c. Impact on the global lee-wave generation

We now apply the results of the 3D simulations to update the global lee-wave generation estimate published by Nikurashin and Ferrari (2011) using a combination of global observations and numerical model output. Specifically, we repeat the same energy conversion calculations as in Nikurashin and Ferrari (2011) but reduce the critical steepness parameter value from 0.7 to 0.4, as estimated here with 3D simulations using realistic topography. The global energy conversion estimate is based on the linear theory expression for the energy conversion and the effective topographic spectrum described in section 2. The theory is applied to abyssal hill topography

obtained from single-beam soundings, bottom stratification estimated from the World Ocean Circulation Experiment (WOCE) hydrography, and bottom geostrophic flows taken from an eddy-resolving global ocean model. Details of the global lee-wave calculation are given in Nikurashin and Ferrari (2011).

The updated map of global energy conversion into internal lee waves is shown in Fig. 8. Comparing this map with that published in Nikurashin and Ferrari (2011), we find that reducing the critical steepness parameter from 0.7 to 0.4 significantly reduces the lee-wave generation in a few regions, but it has a modest global impact. The globally integrated energy conversion drops by 35% from 0.23 to 0.15 TW, well within the uncertainty in the calculation. Most of the reduction occurs in regions with rough topography and weak bottom flows, such as the Mid-Atlantic Ridge, Indian Ocean Ridges, and equatorial Pacific Ocean, characterized by supercritical topography (Fig. 9).

The steepness parameter (Fig. 9) is generally lower in the Southern Ocean than in regions of midocean ridges at low and midlatitudes. While the high values of energy conversion are reduced in Drake Passage, the general pattern and magnitude of lee-wave generation in the Southern Ocean remain largely unchanged. The total
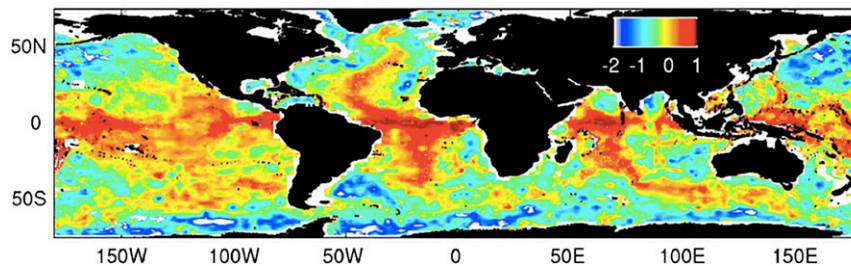
FIG. 9. Global time-averaged topographic steepness parameter (logarithmic scale).

energy conversion into lee waves in the Southern Ocean south of 40°S reduces by 25% from 0.12 to 0.09 TW. Because of the stronger reduction of the energy conversion at low and midlatitudes, the Southern Ocean accounts for 60% of the global lee-wave generation as opposed to the 50% reported in Nikurashin and Ferrari (2011).

Changes in the lee-wave generation in the Drake Passage region are shown in Fig. 10. The time-averaged energy radiation in Drake Passage is reduced by 20%–50% with the strongest reduction in the northern part of Drake Passage. The pattern in reduction tracks the distribution of the steepness parameter. In the northern part of Drake Passage, the steepness parameter values are greater than 0.4 and hence the energy conversion is reduced, while they are generally smaller than 0.4 in the southern part of Drake Passage, south of 60°S.

4. Summary and conclusions

Recent observations in the Southern Ocean report enhanced energy dissipation rates that are significantly smaller than the energy conversion rates predicted by linear theory and idealized 2D simulations. There are a number of mechanisms that can explain the disagreement and need to be considered in the future. In this study, we tested one potential contributor to the overestimation: the finite-amplitude topography effects that result in the suppression of wave radiation and are not represented well by the 2D numerical simulations.

The results showed that energy conversion in 3D simulations saturates, that is, ceases to increase for the increasing steepness of topography, at a critical steepness parameter value of 0.4 (smaller than in the equivalent 2D simulations). The difference between 2D and 3D simulations likely arises from the nonlinear flow-blocking and splitting effects that are not properly captured by the 2D simulations. A better agreement between realistic 3D simulations and recent observations collected in Drake Passage suggests that the lee-wave radiation suppressed in 3D simulations compared

to 2D simulations is more realistic, and hence the 2D nature of topography is crucial to capturing the radiation of lee waves in the ocean. These results are consistent with previous studies in the atmospheric literature (e.g., Welch et al. 2001; Epifanio and Durran 2001; Eckermann et al. 2010). After accounting for 3D effects, observational and model estimates are much closer, and hence it is possible that the 3D effects explain most of the discrepancy and other mechanisms may be less important.

Using a critical steepness parameter value of 0.4 to suppress the energy conversion in an estimate of lee-wave generation for the global ocean, we found that the global energy conversion is reduced by 35% from 0.23 to 0.15 TW, compared to an earlier estimate that used a critical value of 0.7. While this correction is minor on a global scale, energy conversion is significantly reduced regionally in places with rough topography and weak bottom flow, such as the Mid-Atlantic Ridge, Indian Ocean ridges, and equatorial Pacific Ocean, characterized by large supercritical steepness parameters. The reduction of the total energy conversion into lee waves in the Southern Ocean is smaller, 25%, because of the generally smaller values of steepness parameter than at low and midlatitudes.

This work has a number of limitations and we now mention a few that we plan to address in future work. A more direct, quantitative comparison with observations would require better knowledge of the local topography and higher resolution simulations that capture the generation of the waves, their evolution, and breaking. The bottom topography is assumed isotropic here, while it can be strongly anisotropic in some places in the ocean. A study of saturation effects with finite amplitude, *anisotropic* topography would require a larger number of 3D simulations and will be addressed in the future. Finally, the model domain is too short to simulate the interaction of the lee waves reflected at the upper boundary with topography and the advection of the wavefield and turbulence by the ACC, effects that could be also important in the Southern Ocean.
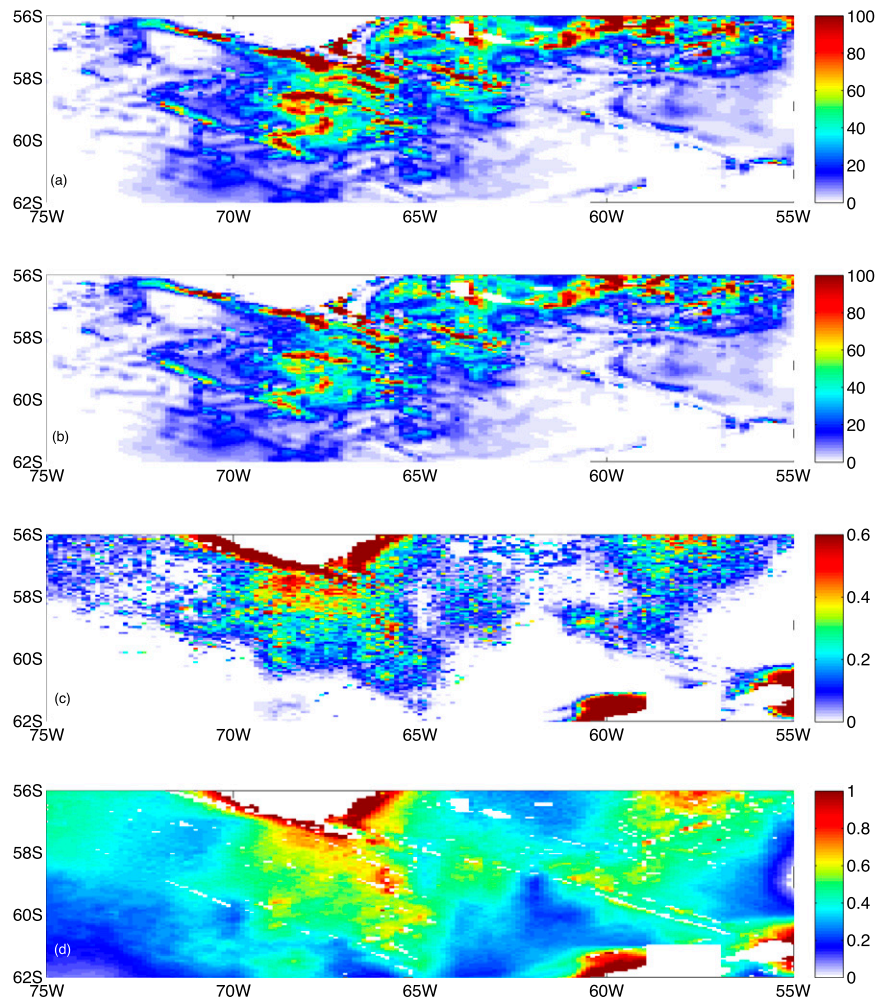
FIG. 10. Time-averaged energy conversion into internal lee waves in Drake Passage $(\mathrm{mW\,m^{-2}})$ (a) adjusted with the critical value of 0.7 based on 2D simulations and (b) adjusted with the critical value of 0.4 based on 3D simulations. (c) Fractional change in the energy conversion, $(E_{0.7} - E_{0.4})/E_{0.7}$. (d) Time-averaged topographic steepness parameter.

REFERENCES

Aguilar, D., and B. Sutherland, 2006: Internal wave generation from rough topography. *Phys. Fluids,* **18,** 066603, doi:10.1063/1.2214538.

Baines, P. G., and R. B. Smith, 1993: Upstream stagnation points in stratified flow past obstacles. *Dyn. Atmos. Oceans,* **18,** 105–113, doi:10.1016/0377-0265(93)90005-R.

Bell, T. H., 1975a: Lee waves in stratified flows with simple harmonic time dependence. *J. Fluid Mech.,* **67,** 705–722, doi:10.1017/S0022112075000560.

——, 1975b: Topographically generated internal waves in the open ocean. *J. Geophys. Res.,* **80,** 320–327, doi:10.1029/JC080i003p00320.

Eckermann, S. D., J. Lindeman, D. Broutman, J. Ma, and Z. Boybeyi, 2010: Momentum fluxes of gravity waves generated by variable Froude number flow over three-dimensional obstacles. *J. Atmos. Sci.,* **67,** 2260–2278, doi:10.1175/2010JAS3375.1.

Epifanio, C. C., and D. R. Durran, 2001: Three-dimensional effects in high-drag-state flows over long ridges. *J. Atmos. Sci.,* **58,** 1051–1065, doi:10.1175/1520-0469(2001)058<1051:TDEIHD>2.0.CO;2.

Garrett, C., and L. St. Laurent, 2002: Aspects of deep ocean mixing. *J. Oceanogr.,* **58,** 11–24, doi:10.1023/A:1015816515476.

Goff, J. A., and T. H. Jordan, 1988: Stochastic modeling of seafloor morphology: Inversion of sea beam data for second-order statistics. *J. Geophys. Res.,* **93,** 13 589–13 608, doi:10.1029/JB093iB11p13589.

Khatiwala, S., 2003: Generation of internal tides in an ocean of finite depth: Analytical and numerical calculations. *Deep-Sea Res. I,* **50,** 3–21, doi:10.1016/S0967-0637(02)00132-2.

Legg, S., and J. Klymak, 2008: Internal hydraulic jumps and overturning generated by tidal flow over a tall steep ridge. *J. Phys. Oceanogr.,* **38,** 1949–1964, doi:10.1175/2008JPO3777.1.

Marshall, J., A. Adcroft, C. Hill, L. Perelman, and C. Heisey, 1997: A finite-volume, incompressible Navier Stokes model for studies of the ocean on parallel computers. *J. Geophys. Res.,* **102,** 5753–5766, doi:10.1029/96JC02775.

Miranda, P. M. A., and I. N. James, 1992: Non-linear three-dimensional effects on gravity-wave drag: Splitting flow and breaking waves. *Quart. J. Roy. Meteor. Soc.,* **118,** 1057–1081, doi:10.1002/qj.49711850803.

Munk, W., and C. Wunsch, 1998: Abyssal recipes II: Energetics of tidal and wind mixing. *Deep-Sea Res.,* **45,** 1977–2010, doi:10.1016/S0967-0637(98)00070-3.

Naveira Garabato, A., K. Heywood, and D. Stevens, 2002: Modification and pathways of Southern Ocean Deep Waters in the Scotia Sea. *Deep-Sea Res.,* **49,** 681–705, doi:10.1016/S0967-0637(01)00071-1.

——, D. Stevens, and K. Heywood, 2003: Water mass conversion, fluxes, and mixing in the Scotia Sea diagnosed by an inverse model. *J. Phys. Oceanogr.,* **33,** 2565–2587, doi:10.1175/1520-0485(2003)033<2565:WMCFAM>2.0.CO;2.

——, K. L. Polzin, B. A. King, K. J. Heywood, and M. Visbeck, 2004: Widespread intense turbulent mixing in the Southern Ocean. *Science,* **303,** 210–213, doi:10.1126/science.1090929.

Nikurashin, M., and R. Ferrari, 2010a: Radiation and dissipation of internal waves generated by geostrophic flows impinging on small-scale topography: Theory. *J. Phys. Oceanogr.,* **40,** 1055–1074, doi:10.1175/2009JPO4199.1.

——, and ——, 2010b: Radiation and dissipation of internal waves generated by geostrophic flows impinging on small-scale topography: Application to the Southern Ocean. *J. Phys. Oceanogr.,* **40,** 2025–2042, doi:10.1175/2010JPO4315.1.

——, and ——, 2011: Global energy conversion rate from geostrophic flows into internal lee waves in the deep ocean. *Geophys. Res. Lett.,* **38,** L08610, doi:10.1029/2011GL046576.

——, and G. Vallis, 2011: A theory of deep stratification and overturning circulation in the ocean. *J. Phys. Oceanogr.,* **41,** 485–502, doi:10.1175/2010JPO4529.1.

——, and R. Ferrari, 2013: Overturning circulation driven by breaking internal waves in the deep ocean. *Geophys. Res. Lett.,* **40,** 3133–3137, doi:10.1002/grl.50542.

——, G. Vallis, and A. Adcroft, 2012: Routes to energy dissipation for geostrophic flows in the Southern Ocean. *Nat. Geosci.,* **6,** 48–51, doi:10.1038/ngeo1657.

Polzin, K. L., and E. Firing, 1997: Estimates of diapycnal mixing using LADCP and CTD data from I8S. *International WOCE Newsletter,* No. 29, WOCE International Project Office, Southampton, United Kingdom, 29–42.

Scott, R. B., J. A. Goff, A. C. Naveira Garabato, and A. J. G. Nurser, 2011: Global rate and spectral characteristics of internal gravity wave generation by geostrophic flow over topography. *J. Geophys. Res.,* **116,** C09029, doi:10.1029/2011JC007005.

Sheen, K. L., and Coauthors, 2013: Rates and mechanisms of turbulent dissipation and mixing in the Southern Ocean: Results from the Diapycnal and Isopycnal Mixing Experiment in the Southern Ocean (DIMES). *J. Geophys. Res.,* **118,** 2774–2792, doi:10.1002/jgrc.20217.

Sloyan, B. M., 2005: Spatial variability of mixing in the Southern Ocean. *Geophys. Res. Lett.,* **32,** L18603, doi:10.1029/2005GL023568.

St. Laurent, L. C., H. L. Simmons, and S. R. Jayne, 2002: Estimating tidally driven mixing in the deep ocean. *Geophys. Res. Lett.,* **29,** 2106, doi:10.1029/2002GL015633.

——, A. C. Naveira Garabato, J. Ledwell, A. M. Thurnherr, J. M. Toole, and A. J. Watson, 2012: Turbulence and diapycnal mixing in Drake Passage. *J. Phys. Oceanogr.,* **42,** 2143–2152, doi:10.1175/JPO-D-12-027.1.

Waterman, S., A. Naveira Garabato, and K. Polzin, 2012: Internal waves and turbulence in the Antarctic Circumpolar Current. *J. Phys. Oceanogr.,* **43,** 259–282, doi:10.1175/JPO-D-11-0194.1.

Welch, W., P. Smolarkiewicz, R. Rotunno, and B. Boville, 2001: The large-scale effects of flow over periodic mesoscale topography. *J. Atmos. Sci.,* **58,** 1477–1492, doi:10.1175/1520-0469(2001)058<1477:TLSEOF>2.0.CO;2.

Wunsch, C., 1998: The work done by the wind on the oceanic general circulation. *J. Phys. Oceanogr.,* **28,** 2332–2340, doi:10.1175/1520-0485(1998)028<2332:TWDBTW>2.0.CO;2.